Why rogue waves occur atop abrupt depth transitions

Li, Yan; Draycott, Samuel; Zheng, Yaokun; Lin, Zhiliang; Adcock, Thomas A.A.; Van Den Bremer, Ton S.

Important note
To cite this publication, please use the final published version (if applicable).
Please check the document version above.

CrossMark

Why rogue waves occur atop abrupt depth transitions

Yan Li[1,2,†], Samuel Draycott[3], Yaokun Zheng[4], Zhiliang Lin[4], Thomas A.A. Adcock[1] and Ton S. van den Bremer[1,5]

[1]Department of Engineering Science, University of Oxford, Parks Road, Oxford OX1 3PJ, UK

[2]Department of Energy and Process Engineering, Norwegian University of Science and Technology, N-7491 Trondheim, Norway

[3]Department of Mechanical, Aerospace and Civil Engineering, University of Manchester, Manchester M13 9PL, UK

[4]State Key Laboratory of Ocean Engineering, School of Naval Architecture, Ocean and Civil Engineering, Shanghai Jiao Tong University, Shanghai 200240, PR China

[5]Faculty of Civil Engineering and Geosciences, Delft University of Technology, 2628 CD Delft, The Netherlands

Abrupt depth transitions (ADTs) have recently been identified as potential causes of 'rogue' ocean waves. When stationary and (close-to-) normally distributed waves travel into shallower water over an ADT, distinct spatially localized peaks in the probability of extreme waves occur. These peaks have been predicted numerically, observed experimentally, but not explained theoretically. Providing this theoretical explanation using a leading-order-physics-based statistical model, we show, by comparing to new experiments and numerical simulations, that the peaks arise from the interaction between linear free and second-order bound waves, also present in the absence of the ADT, and new second-order free waves generated due to the ADT.

1. Introduction

Different physical mechanisms have been proposed to explain so-called 'rogue' waves on the surface of the ocean (Dysthe, Krogstad & Müller 2008; Kharif, Pelinovsky & Slunyaev 2008; Onorato *et al.* 2013; Adcock & Taylor 2014; Dudley *et al.* 2019). Rogue waves are typically defined as large waves whose height exceeds the significant wave height by a factor of 2–2.2 (Kharif *et al.* 2008). Such waves are of increased interest if they

† Email address for correspondence: yan.li@ntnu.no

occur more frequently than predicted by a Gaussian process. A useful proxy for rogue waves therefore is the excess kurtosis of the free surface relative to a Gaussian process (Mori & Janssen 2006). Physical mechanisms proposed include random linear dispersive focusing enhanced by weak bound-wave nonlinearity (Fedele *et al.* 2016), modulational or Benjamin–Feir instability in deep water (Benjamin & Feir 1967; Janssen 2003), and abrupt depth transitions (ADTs), among others.

Recently, several authors have shown that rogue waves can form at the top of ADTs for waves in shallow to intermediate depth, as reviewed in Trulsen *et al.* (2020). In the experiments of Trulsen, Zeng & Gramstad (2012), local peaks of skewness and kurtosis occurred a short distance after a $1:20$ underwater slope when waves travelled from a deeper to a shallower domain (see also Zhang *et al.* 2019). Similar peaks have been observed experimentally for shoals (Ma, Dong & Ma 2014; Trulsen *et al.* 2020) and steps (Bolles, Speer & Moore 2019). Local peaks in skewness and kurtosis have also been predicted using reduced-form nonlinear evolution equations, such as the Korteweg–de Vries equation for variable shallow depth (Sergeeva, Pelinovsky & Talipova 2011; Majda, Moore & Qi 2019) and the Boussinesq equations (Gramstad *et al.* 2013; Kashima, Hirayama & Mori 2014; Zhang *et al.* 2019), and by fully nonlinear numerical simulations of the water wave equations (Viotti & Dias 2014; Ducrozet & Gouin 2017; Zheng *et al.* 2020; Zhang & Benoit 2021). The magnitude of the peaks is greatest when the ADT is infinitely steep, i.e. a step (Zheng *et al.* 2020). Peaks in skewness and kurtosis only occur for sufficiently shallow depths (Trulsen *et al.* 2020; Zheng *et al.* 2020), corresponding to a depth beyond the applicability of the nonlinear Schrödinger equation (Zeng & Trulsen 2012), which correctly predicts the absence of peaks in deeper water (Lawrence, Trulsen & Gramstad 2021).

Two hypotheses have been proposed to explain these peaks. According to the first, ADTs place the system out of equilibrium; the peaks are the response of a system that rapidly adjusts to a new equilibrium driven by nonlinear processes (third- and higher-order in steepness) (Trulsen 2018; Viotti & Dias 2014). According to the second hypothesis, the peaks are formed by second-order effects in steepness (Gramstad *et al.* 2013; Ducrozet & Gouin 2017; Zhang *et al.* 2019; Zheng *et al.* 2020), but the mechanism by which this occurs is not clear.

We develop a statistical model, based on the second-order theory for wave propagation over a step that was developed in Li *et al.* (2021*b*) and validated experimentally in Li *et al.* (2021*a*), that can accurately predict the magnitude and location of the peaks in kurtosis atop ADTs. Our model confirms the validity of the second hypothesis and demonstrates that the underlying mechanism is one of the interplay between linear free and second-order bound waves, which are also present in the absence of the ADT, and the second-order free waves generated due to the ADT.

2. Theoretical model

2.1. *Deterministic model (Li et al. 2021b)*

Our starting point is the deterministic model of Li *et al.* (2021*b*) for wave group propagation over a step. We consider weakly nonlinear unidirectional water waves on the surface of a constant-density fluid, ignoring surface tension and viscosity, so that the fluid satisfies potential flow. The ADT (cf. figure 1) takes the form of a discontinuity or 'step' in water depth $h(x)$ at $x = 0$, where h changes from h_d for $x < 0$ to a shallower value h_s for $x > 0$, with x denoting the horizontal axis. We consider intermediate water depths ($O(kh) = 1$ with k the wavenumber) and leading-order approximations to the water
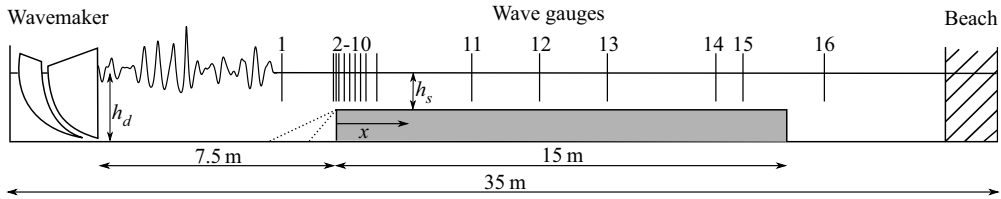
Figure 1. Experimental set-up.

wave equations. Specifically, as in the classical statistical models of Tayfun ([1980](#), [1986](#)), the solutions are valid up to second order in steepness $\epsilon = k_0 A_0$, where k_0 and A_0 denote the characteristic wavenumber and amplitude, respectively, and narrow-banded or valid up to first order in the dimensionless bandwidth parameter, defined as $\delta = 1/(k_0 \sigma_0)$ with σ_0 the characteristic group length.

2.1.1. *Incident wave field*

The surface elevation of the incident wave field travelling towards the ADT can be obtained from a combined Stokes and multiple-scales expansion (e.g. Mei, Stiassnie & Yue [1989](#)):

$$\zeta(x,t) = \zeta^{(1)}(x,t) + \zeta^{(2)}(x,t) \quad \text{for } x < 0, \text{ with} \tag{2.1a}$$

$$\zeta^{(1)}(x,t) = A \cos \psi_0(x,t) \quad \text{and} \quad \zeta^{(2)}(x,t) = k_0 A^2 [C_{20,b} + C_{22,b} \cos 2\psi_0(x,t)], \tag{2.1b}$$

where the superscripts denote the order in ϵ; $A(x,t)$ the envelope; and $\psi_0 = k_0 x - \omega_0 t + \theta_0$ the phase, with k_0 the carrier wavenumber and $\omega_0 = \omega(k_0, h_d)$ the angular velocity obeying linear dispersion, $\omega(k,h) = \sqrt{gk \tanh kh}$ with g gravitational acceleration, and θ_0 the phase. The envelope $A(x,t) = A(x/c_{g0} - t)$ travels at the group velocity $c_{g0} = c_g(k_0, h_d)$, with $c_g(k,h) = (\omega/(2k))(1 + 2kh/\sinh 2kh)$. The coefficients of the bound second-order sub-harmonic and super-harmonic waves are (e.g. Mei *et al.* [1989](#))

$$C_{20,b}(kh) = [(2gh - c_g^2)/(2 \sinh 2kh) + 2gc_g/\omega]/[4(c_g^2 - gh)], \tag{2.2a}$$

$$C_{22,b}(kh) = \cosh kh (2 \cosh^2 kh + 1)/(4 \sinh^3 kh), \tag{2.2b}$$

where $C_{20,b}(k_0 h_d)$ and $C_{22,b}(k_0 h_d)$ are the coefficients in ([2.1](#)), and we have further assumed the envelope is long relative to the water depth (as in Mei *et al.* [1989](#)).

2.1.2. *Transmitted wave field*

Upon reaching the ADT ($x = 0$), the incident wave field is reflected and transmitted. We focus on the latter here. At first order in ϵ, the carrier wave on the shallower side travels at speed $c_{g0s} = c_g(k_{0s}, h_s)$, where k_{0s} denotes the wavenumber that can be found by solving $\omega_0 = \omega(k_{0s}, h_s)$ and corresponds to a shorter wavelength. In addition, evanescent waves are generated in the vicinity of the step that vanish exponentially with distance away from the step. At second order in ϵ, the sub-harmonic and super-harmonic bound waves associated with the transmitted wave field must change magnitude at the step, and additional free sub-harmonic and super-harmonic waves are generated, which, respectively, travel at the shallow-water speed $\sqrt{gh_s}$ or satisfy the linear dispersion relation for $\omega(k_{20s}, h_s) = 2\omega_0$ with k_{20s} the wavenumber of the super-harmonic waves.

Based on Massel ([1983](#)), who derived expressions for both linear and second-order super-harmonic components for a monochromatic wave, and Li *et al.* ([2021*b*](#)), who

extended this work to narrow-banded wavepackets, the surface elevation on the shallower side (i.e. for $x > 0$) is given by (Li *et al.* 2021*b*)

$$\zeta_s(x, t) = \zeta_s^{(1)}(x, t) + \zeta_s^{(2)}(x, t) \quad \text{for } x > 0, \tag{2.3a}$$

with

$$\zeta_s^{(1)}(x, t) = A_s(x, t) \cos \psi_{0s} + \zeta_{Es}^{(1)}, \quad A_s(x, t) = |T_0| A \left(x/c_{g0s} - t\right), \tag{2.3b}$$

$$\zeta_s^{(2)}(x, t) = \zeta_s^{(20)} + \zeta_s^{(22)}, \tag{2.3c}$$

$$\zeta_s^{(20)}(x, t) = C_{20,b} k_{0s} A_s^2 + C_{20,f} k_{0s} |T_0|^2 A^2 (x/\sqrt{gh_s} - t) + \zeta_{Es}^{(20)}, \tag{2.3d}$$

and

$$\zeta_s^{(22)}(x, t) = C_{22,b} k_{0s} A_s^2 \cos(2\psi_{0s}) + C_{22,f} k_{0s} |T_0|^2 A^2 (x/c_{g22s} - t) \cos(2\psi_{0s} + \psi_{22,f})$$
$$+ \zeta_{Es}^{(22)}, \tag{2.3e}$$

in which T_0 denotes the complex transmission coefficient, and the subscripts E, b and f denote the evanescent, bound and free waves, respectively. In the first-order term, $\psi_{0s}(x, t) = \psi_0(x, t) + (k_{0s} - k_0)x + \theta_{T_0}$ with θ_{T_0} denoting the phase shift due to the step ($\theta_{T_0} = \arg(T_0)$). The second-order bound wave coefficients can be evaluated from (2.2): $C_{20,b}(k_{0s}h_s)$, $C_{22,b}(k_{0s}h_s)$. The second-order free wave coefficients are given by $C_{20,f} = |T_{20,f}|/|T_0|^2$ and $C_{22,f} = 2\omega_0^2|T_{22,f}|/(gk_{0s}|T_0|^2)$ with $T_{20,f}$ and $T_{22,f}$ the (complex) coefficients for the sub- and super-harmonic free wave, respectively. T_0, T_{20} and $T_{22,f}$ are obtained from the boundary conditions at the step (see Li *et al.* (2021*b*) for details). In the second-order terms, $c_{g22s} = c_g(k_{20s}, h_s)$ is the group velocity of the free super-harmonic envelope, and $\psi_{22,f}(x) = k_{20s}x - 2k_{0s}x + \theta_{T_{22,f}} - 2\theta_{T_0}$ denotes the phase of the free super-harmonic waves relative to the bound super-harmonic waves, with $\theta_{T_{22,f}}$ the phase shift of the free super-harmonic waves upon transmission ($\theta_{T_{22,f}} = \arg(T_{22,f})$). To obtain tractable solutions, Li *et al.* (2021*b*) ignore forcing by (small) products of linear evanescent waves.

2.2. *A new statistical model*

To develop a statistical model based on the deterministic model of Li *et al.* (2021*b*) outlined in § 2.1, we assume a normally distributed linear incident field $\tilde{\zeta}^{(1)}$ with variance μ_0, which is both stationary and homogeneous (for $x < 0$). Specifically, we define a Rayleigh-distributed envelope $\tilde{A}$ and a uniformly distributed phase $\tilde{\psi}$, so that $\tilde{\zeta}^{(1)} = \tilde{A} \cos(\tilde{\psi})$. Tildes denote random variables. The incident wave field on the deeper side ($x < 0$) becomes (cf. (2.1))

$$\tilde{\zeta} = \tilde{\zeta}^{(1)} + \tilde{\zeta}^{(2)} \text{ for } x < 0, \quad \tilde{\zeta}^{(1)} = \tilde{A} \cos \tilde{\psi}, \quad \text{and} \quad \tilde{\zeta}^{(2)} = k_0 \tilde{A}^2 [C_{20,b} + C_{22,b} \cos 2\tilde{\psi}]. \tag{2.4a-c}$$

Neglecting the effect of evanescent waves, we obtain on the shallower side (cf. (2.3))

$$\tilde{\zeta}_s = \tilde{\zeta}_s^{(1)} + \tilde{\zeta}_s^{(2)} \quad \text{for } x > 0, \tag{2.5a}$$

with

$$\tilde{\zeta}_s^{(1)} = |T_0| \tilde{A} \cos(\tilde{\psi}_{0s}) \quad \text{and} \quad \tilde{\zeta}_s^{(2)}(x) = \tilde{\zeta}_s^{(20)}(x) + \tilde{\zeta}_s^{(22)}(x), \tag{2.5b}$$

$$\tilde{\zeta}_s^{(20)}(x) = k_{0s}|T_0|^2 \tilde{A}^2 \left(C_{20,b} + C_{20,f} R_{20}(x)\right), \quad \tilde{\psi}_{0s} = \tilde{\psi} + (k_{0s} - k_0)x + \theta_{T_0}, \tag{2.5c}$$

and

$$\zeta_s^{(22)}(x) = k_{0s}|T_0|^2\tilde{A}^2[C_{22,b}\cos(2\tilde{\psi}_{0s}) + C_{22,f}R_{22}(x)\cos(2\tilde{\psi}_{0s} + \psi_{22,f}(x))], \quad (2.5d)$$

where $R_{20}(x)$ and $R_{22}(x)$ are envelope functions, obtained by expanding the envelope of the sub- and super-harmonic waves, respectively, about the centre of the transmitted envelope. They can be expressed in terms of the focused deterministic envelope A as

$$R_{20}(x) = A^2(x/\sqrt{gh_s} - x/c_{g0s})/A^2(0), \quad R_{22}(x) = A^2(x/c_{g22s} - x/c_{g0s})/A^2(0), \quad (2.6a,b)$$

where $A(0)$ is the central magnitude of the deterministic envelope. The focused deterministic envelope can be obtained from the energy spectrum $S(\omega)$ by $A(t) = \int \sqrt{2S(\omega)}\cos((\omega - \omega_0)t)\,d\omega$. For a Gaussian deterministic envelope $A = a_0 \exp(-c_{g0}^2(x/c_{g0s} - t)^2/(2\sigma_0^2))$, we obtain $R_{20}(x) = \exp[-(c_{g0}x/\sqrt{gh_s} - c_{g0}x/c_{g0s})^2/\sigma_0^2]$ and $R_{22}(x) = \exp[-(c_{g0}x/c_{g22s} - c_{g0}x/c_{g0s})^2/\sigma_0^2]$. A long distance away from the step, $R_{20}, R_{22} \to 0$, and we recover the standard homogeneous result for constant depth (e.g. Tayfun 1986).

2.2.1. *Statistical properties*

The skewness $s = \langle(\tilde{\zeta}_s - m)^3\rangle/v^{3/2}$ and kurtosis $\kappa = \langle(\tilde{\zeta}_s - m)^4\rangle/v^2$ of the random surface elevation can be directly obtained from (2.5) with $m = \langle\tilde{\zeta}_s\rangle$, $v = \langle(\tilde{\zeta}_s - m)^2\rangle$ and $\langle\cdots\rangle$ the combined expectation operator of the random variables $\tilde{A}$ and $\tilde{\psi}$:

$$s = 6k_{0s}\sqrt{\mu_{0s}}C_2(x) + O(\mu_{0s}^{3/2}), \quad (2.7)$$

$$\kappa = 3 + 24k_{0s}^2\mu_{0s}\left(\kappa_{2,b} + \kappa_{2,bf}(x) + \kappa_{2,f}(x)\right) + O(\mu_{0s}^2). \quad (2.8)$$

Here $\mu_{0s} = |T_0|^2\mu_0$ denotes the variance of the surface elevation on the shallower side, $C_2(x) = C_{20,b} + C_{22,b} + C_{20,f}R_{20}(x) + C_{22,f}R_{22}(x)\cos\psi_{22,f}(x)$, $\kappa_{2,b}$ captures the contribution to kurtosis by bound waves, $\kappa_{2,f}$ by free waves and $\kappa_{2,bf}$ by their combination:

$$\kappa_{2,b} = 3C_{20,b}^2 + 4C_{20,b}C_{22,b} + 3C_{22,b}^2, \quad (2.9a)$$

$$\kappa_{2,f}(x) = 3C_{20,f}^2R_{20}^2 + 4C_{20,f}C_{22,f}R_{20}R_{22}\cos\psi_{22,f} + 3C_{22,f}^2R_{22}^2, \quad (2.9b)$$

$$\kappa_{2,bf}(x) = (6C_{20,b} + 4C_{22,b})(C_{20,f}R_{20} + C_{22,f}R_{22}\cos\psi_{22,f}). \quad (2.9c)$$

From (2.5), we can also obtain a second-order accurate expression for wave crests $\tilde{\zeta}_c$:

$$\tilde{\zeta}_c(x) = |T_0|\tilde{A} + k_{0s}|T_0|^2\tilde{A}^2C_2(x). \quad (2.10)$$

In non-dimensional form, $\tilde{\xi}_c = \tilde{\zeta}_c/H_{ss}$ with $H_{ss} = 4\sqrt{\mu_{0s}}$ the significant wave height on the shallower side, the crest elevation has the probability density function (cf. Tayfun 1980)

$$f_{\tilde{\xi}_c}(\xi_c) = \frac{16u\exp(-8u^2)}{1 + 4\epsilon_s C_2(x)u} \quad \text{with } u = \frac{\sqrt{1 + 8\epsilon_s C_2(x)\xi_c} - 1}{4\epsilon_s C_2(x)}, \quad (2.11a,b)$$

and $\epsilon_s = k_{0s}H_{ss}/2$ measures steepness in a random sea. Equation (2.11a,b) can be integrated to obtain the exceedance probability (cf. Forristall 2000),

$$P(\tilde{\xi}_c > \xi_c) = \exp(-8u^2(\xi_c)). \quad (2.12)$$

As $\epsilon_s \to 0$, we recover from (2.11a,b) and (2.12) the Rayleigh distribution. If the contributions by the second-order free waves are neglected, which is valid in the absence

of, or a long distance away from, a step, then $R_{20} \rightarrow 0$ and $R_{22} \rightarrow 0$, and (2.5), (2.7), (2.8) and (2.10) reduce to the second-order accurate result for constant depth (Tayfun 1980, 1986).

2.2.2. *Rogue wave generating mechanism*

As described in § 2.1.2, second-order sub- and super-harmonic free waves are released upon transmission over the ADT. On the shallower side, these free waves coexist with the transmitted linear free waves and their second-order bound waves, which would also be present for constant depth. Compared to the second-order statistical model for constant depth (Tayfun 1980, 1986), the additional second-order free waves lead to an increased likelihood of large waves atop the ADT. The likelihood of large waves is enhanced by the presence of sub-harmonic free waves ($C_{20,f} > 0$) and beating between the bound and free super-harmonics, which results in local maxima (Li *et al.* 2021*b*). Both these effects only occur near the top of an ADT, where the second-order free waves are initially generated and where their envelopes still overlap with the linear envelope. Since both sub-harmonics and super-harmonics propagate at different group speed from the linear envelope, they separate over a sufficient distance away from the step. This mechanism locally amplifies skewness (2.7), kurtosis (2.8) and exceedance probability of crests (2.12).

3. Results

3.1. *Experiments and numerical simulations*

To validate our statistical model, we performed laboratory experiments and fully nonlinear numerical simulations. Experiments were carried out in the Coastal, Ocean and Sediment Transport (COAST) Laboratory at the University of Plymouth, UK. A schematic of the experimental set-up (and the numerical wave tank) is shown in figure 1. Two water depths on the deeper side were used: $h_d = 0.55$ m and $h_d = 0.75$ m. Hence, the water depth on the shallower side is $h_s = h_d - 0.35$ m. The numerical wave tank (Zheng *et al.* 2020) is equivalent to that of the laboratory except that the computational domain has a total length of $50\lambda_0$, where λ_0 denotes the carrier wavelength on the deeper side, with a length of $20\lambda_0$ on the deeper side ($x < 0$) and $30\lambda_0$ on the shallower side ($x > 0$).

In both the experiments and the numerics, the (linear) wavemaker was programmed to generate irregular waves based on JONSWAP spectra for different peak frequencies f_p and water depths (peak enhancement factor $\gamma = 3.3$). Four cases are examined with parameters presented in table 1. Cases A and C start in deeper water ($k_0 h_d = 1.6$) compared to B and D ($k_0 h_d = 1.0, 1.1$), and cases A and B ($k_0 h_d/(k_{0s} h_s) = 1.9, 1.8$) experience a larger depth transition than C and D ($k_0 h_d/(k_{0s} h_s) = 1.6, 1.5$). We examine skewness and kurtosis (§ 3.2), followed by wave crest distribution (§ 3.3).

For each case in table 1, several realizations with different randomized amplitudes and phases were generated in both experiments and numerical simulations. Random amplitudes and phases are generated for each frequency component as described in § 2.2. Each of these realizations was $\sim$20 min (1200 s), with frequency spacing $\Delta f = 1/1800$ Hz. The parameters used as input to the statistical model are estimated from the experimental values measured at the first gauge, before the step. For our (narrow-banded) model predictions, we have used an estimated, equivalent Gaussian envelope A to compute the envelope functions $R_{20}(x)$ and $R_{22}(x)$.

Case	f_p (Hz)	h_d (m)	$k_0 h_d$	$k_{0s} h_s$	H_{m0} (m)	δ	H_s (m)	ϵ	$\Gamma(k_0 h_d)$	$\Gamma(k_{0s} h_s)$	N_1	N_2
A	0.80	0.55	1.6	0.79	0.046	0.12	0.040	0.057	0.0097	0.19	14	14
B	0.60	0.55	1.0	0.57	0.035	0.24	0.029	0.027	0.019	0.26	14	14
C	0.70	0.75	1.6	1.0	0.078	0.22	0.069	0.074	0.013	0.12	8	14
D	0.55	0.75	1.1	0.76	0.079	0.22	0.069	0.052	0.036	0.20	9	14

Table 1. Parameters of the laboratory experiments and fully nonlinear numerical simulations. The shallower water depth is $h_s = h_d - 0.35$ m; the bandwidth is $\delta = 1/(k_0 \sigma_0)$; H_{m0} is the measured significant wave height of the entire signal (the table shows its value obtained at the first gauge on the deeper side); $H_s = 4\sqrt{\mu_0}$ is the significant wave height of the linearized surface elevation on the deeper side; the steepness is $\epsilon = k_0 H_s / 2$; $\Gamma(kh) = \epsilon C_{22b}(kh)/(kh)^3$ denotes a parameter that measures the degree of nonlinearity relative to depth (Toffoli *et al.* 2007), with $C_{22,b}$ defined by (2.2*b*); and N_1 and N_2 denote the total number of the random realizations per case in experiments and numerical simulations, respectively.
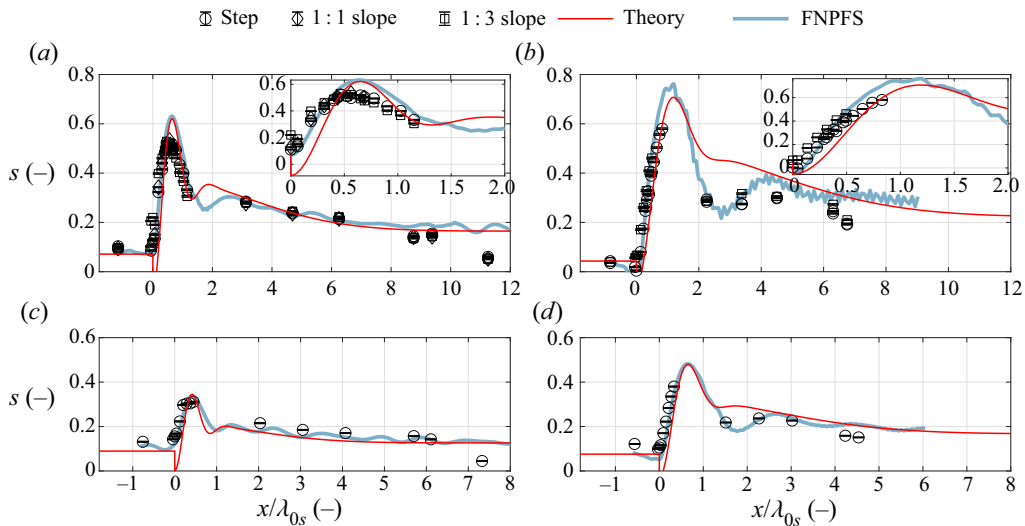

Figure 2. Spatial variation of skewness *s*, comparing theoretical prediction by (2.7), experiments and numerical simulations ('FNPFS') with λ_{0s} the peak wavelength (step at $x = 0$). The (small) error bars for the experiments and the thickness of the blue line for the numerics denote $\pm$ one standard deviation either side of the mean. Panels (*a*–*d*) correspond to the cases in table 1.

3.2. *Skewness and kurtosis*

Figure 2 shows the spatial variation of skewness either side of the ADT ($x = 0$) for the four cases in table 1, including the step and the $1:1$ and $1:3$ slopes (for cases A and B). In all cases, the transition to a higher equilibrium value of skewness associated with larger bound waves for shallower depth is associated with sharp peaks. These sharp peaks, observed in previous studies, occur within one wavelength of the step. Their magnitudes and locations in both experiments and numerics, which are in good agreement, are predicted well by our statistical model. The non-uniform spatial resolution of experimental values is due to the limited number of gauges. We do not observe a significant difference between the experiments for a step and the $1:1$ and $1:3$ slopes, implying that the physics of steep slopes is captured well by our model. The largest peak is observed when the depth before the step is shallowest and the depth transition is greatest (case B).
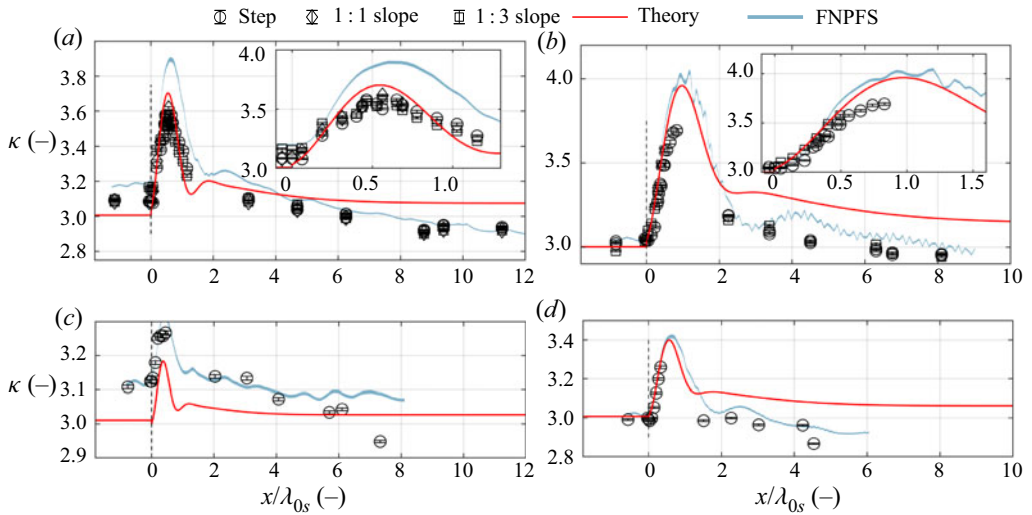
Figure 3. Spatial variation of kurtosis κ, comparing theoretical prediction by (2.8), experiments and numerical simulations ('FNPFS') with λ_{0s} the peak wavelength (step at $x = 0$). The (small) error bars for the experiments and the thickness of the blue line for the numerics denote $\pm$ one standard deviation either side of the mean. Panels (*a–d*) correspond to the cases in table 1.

The only significant difference between the numerical simulations and our model in figure 2 arises in the region after the first peak, where we have few experimental observations (cases B and D), which agree better with the numerical simulations. These differences are likely due to violation of the narrow bandwidth assumption in our model for the broad-banded JONSWAP spectra we have used in the interest of realism, which causes the smearing out of the super-harmonic beating pattern. Figure 3 shows the spatial variation of kurtosis either side of the ADT ($x = 0$) for cases A–D. In all cases, the transmission over the ADT is associated with sharp peaks in kurtosis. In principle, two processes can contribute to kurtosis: third-order processes associated with modulational (in)stability that drive build-up of phase correlation of the linear signal (Janssen 2003) on the one hand and second-order bound and free waves on the other hand; both are captured by the experiments and the numerical simulations but only the latter by our statistical model. In the cases that are modulationally unstable before the ADT (A and C with $k_0 h_d = 1.6 > 1.36$), the kurtosis in experiments and numerics starts slightly above the linear Gaussian value of 3 with a negligible contribution by second-order bound waves. In all cases, the kurtosis in experiments and numerics gradually decays to an equilibrium value slightly below 3 to the right of the ADT, corresponding to the modulationally stable conditions on the shallower side ($k_{0s} h_s < 1.36$), where our second-order accurate statistical model only predicts a small positive contribution to kurtosis by bound waves ($R_{20} = R_{22} = 0$ for $x \gg \sigma_{0s}$ with $\sigma_{0s} = \sigma_0 c_{g0s}/c_{g0}$).

Crucially, the locations of the peaks in kurtosis are predicted accurately by our (second-order accurate) model in all cases. So are their magnitudes, with the relatively small differences between numerics and our model potentially arising because of third-order effects not included in our model, except for the deepest of our cases (case C, with $k_s h_d = 1.6$, $k_{0s} h_s = 1.0$), for which these third-order effects are of the same order of magnitude as the (small) second-order peaks predicted by our model. Peaks are more significant when the water depth is shallower and the depth transition is greater. The kurtosis for the step and the $1:1$ and $1:3$ slopes is not significantly different.
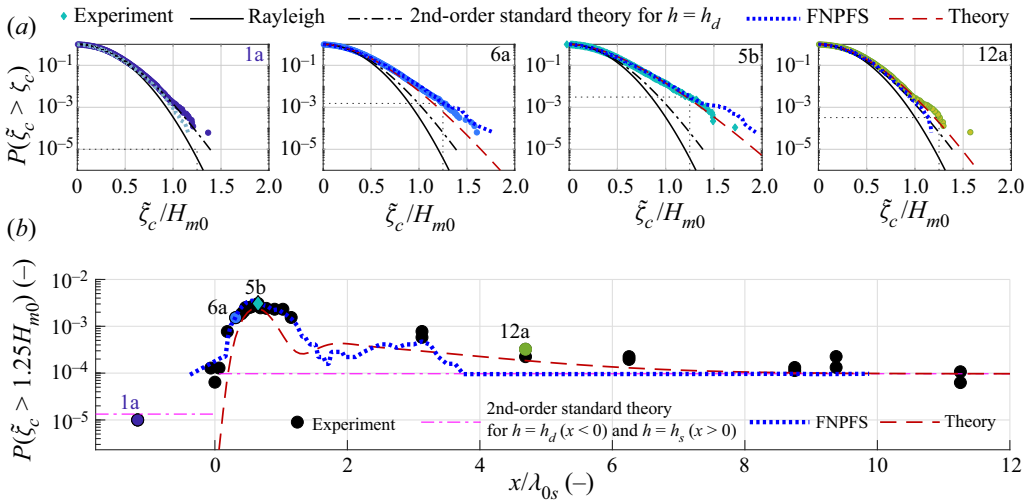
919 R5-8

Figure 4. Crest exceedance probability distribution at four locations (*a*) and the probability of rogue waves as a function of space (*b*) for case A, comparing the theoretical prediction by (2.12), experiments and numerical simulations ('FNPFS') (step at $x = 0$).

3.3. *Wave crest distribution*

Figure 4 shows the exceedance probability distribution and the spatial variation of the probability of rogue waves, defined here as $P(\tilde{\zeta}_c > 1.25H_{m0})$ with H_{m0} the measured significant wave height (of the entire signal), for case A (similar results are obtained for cases B–D). Very good agreement between the experiments, numerical simulations and theory is evident. In particular, the agreement is clear at the location of maximum rogue wave probability (gauge 5b). Minor differences in the rogue wave probability between, on the one hand, the theoretical predictions and, on the other hand, the experiments and numerics, which are in better agreement, can be observed close to the ADT ($0 < x/\lambda_{0s} \lesssim 0.2$) and after the peak ($1 \lesssim x/\lambda_{0s} \lesssim 3$). The former is likely due to evanescent waves being neglected in our model, whereas the latter is primarily a result of the narrow-bandwidth assumption we have made (see Li *et al.* 2021*b*).

4. Conclusions

We have presented a statistical model to explain why rogue waves occur atop abrupt depth transitions (ADTs) in intermediate water depth. The model, based on Massel (1983) and Li *et al.* (2021*b*), includes nonlinearity up to second order in steepness, assumes narrow-banded irregular waves, represents the ADT as an infinitely steep step, and ignores the role of evanescent waves. We have validated our model through comparison to laboratory experiments and fully nonlinear numerical simulations of the water wave equations. In doing so, we have explained the mechanism behind the sharp peaks in kurtosis, indicative of rogue waves, atop ADTs recently observed by a large number of authors in experiments and numerical simulations (see e.g. Trulsen *et al.* (2020) and references therein). We show that peaks in kurtosis arise from the coexistence of linear free and second-order bound waves, which are also present in the absence of the ADT, and the second-order free waves additionally generated due to the ADT. As the second-order free waves always overlap with the linear waves near the top of the ADT but travel at different phase and group speeds (from the linear waves), the peaks are localized and the total

wave field becomes inhomogeneous. Compared to (realistically broad-banded) numerical simulations and experiments, our (narrow-banded) model provides an accurate prediction of the spatially varying probability distribution of rogue waves and the associated peaks in skewness and kurtosis atop ADTs and identifies and explains a new physical mechanism by which rogue waves can arise in the ocean.

Declaration of interests. The authors report no conflicts of interest.

Author ORCIDs.

Ⓓ Yan Li https://orcid.org/0000-0001-8925-3749;

Ⓓ Samuel Draycott https://orcid.org/0000-0002-7372-980X;

Ⓓ Thomas A.A. Adcock https://orcid.org/0000-0001-7556-1193;

Ⓓ Ton S. van den Bremer https://orcid.org/0000-0001-6154-3357.

REFERENCES

ADCOCK, T.A.A. & TAYLOR, P.H. 2014 The physics of anomalous ('rogue') ocean waves. *Rep. Prog. Phys.* **77** (10), 105901.

BENJAMIN, T.B. & FEIR, J.E. 1967 The disintegration of wave trains on deep water Part 1. Theory. *J. Fluid Mech.* **27** (3), 417–430.

BOLLES, C.T., SPEER, K & MOORE, M.N.J. 2019 Anomalous wave statistics induced by abrupt depth change. *Phys. Rev. Fluids* **4** (1), 011801.

DUCROZET, G. & GOUIN, M. 2017 Influence of varying bathymetry in rogue wave occurrence within unidirectional and directional sea-states. *J. Ocean Engng* **3** (4), 309–324.

DUDLEY, J.M., GENTY, G., MUSSOT, A., CHABCHOUB, A. & DIAS, F. 2019 Rogue waves and analogies in optics and oceanography. *Nat. Rev. Phys.* **1** (11), 675–689.

DYSTHE, K.B., KROGSTAD, H.E. & MÜLLER, P. 2008 Oceanic rogue waves. *Annu. Rev. Fluid Mech.* **40**, 287–310.

FEDELE, F., BRENNAN, J., DE LEÓN, S.P., DUDLEY, J. & DIAS, F. 2016 Real world ocean rogue waves explained without the modulational instability. *Sci. Rep.* **6**, 27715.

FORRISTALL, G.Z. 2000 Wave crest distributions: observations and second-order theory. *J. Phys. Oceanogr.* **30** (8), 1931–1943.

GRAMSTAD, O., ZENG, H., TRULSEN, K. & PEDERSEN, G.K. 2013 Freak waves in weakly nonlinear unidirectional wave trains over a sloping bottom in shallow water. *Phys. Fluids* **25** (12), 122103.

JANSSEN, P.A.E.M. 2003 Nonlinear four-wave interactions and freak waves. *J. Phys. Oceanogr.* **33**, 863–884.

KASHIMA, H., HIRAYAMA, K. & MORI, N. 2014 Estimation of freak wave occurrence from deep to shallow water regions. *Coast. Engng* **1** (34), 36.

KHARIF, C., PELINOVSKY, E. & SLUNYAEV, A. 2008 *Rogue Waves in the Ocean.* Springer Science & Business Media.

LAWRENCE, C., TRULSEN, K. & GRAMSTAD, O. 2021 Statistical properties of wave kinematics in long-crested irregular waves propagating over non-uniform bathymetry. *Phys. Fluids* **33** (4), 046601.

LI, Y., DRAYCOTT, S., ADCOCK, T.A.A. & VAN DEN BREMER, T.S. 2021*a* Surface wavepackets subject to an abrupt depth change. Part II: experimental analysis. *J. Fluid Mech.* **915**, A72.

LI, Y., ZHENG, Y.K., LIN, Z.L., ADCOCK, T.A.A. & VAN DEN BREMER, T.S. 2021*b* Surface wavepackets subject to an abrupt depth change. Part I: second-order theory. *J. Fluid Mech.* **915**, A71.

MA, Y.X., DONG, G. & MA, X. 2014 Experimental study of statistics of random waves propagating over a bar. *Coast. Engng* **1** (34), 30.

MAJDA, A.J., MOORE, M.N.J. & QI, D. 2019 Statistical dynamical model to predict extreme events and anomalous features in shallow water waves with abrupt depth change. *Proc. Natl Acad. Sci. USA* **116** (10), 3982–3987.

MASSEL, S.R. 1983 Harmonic generation by waves propagating over a submerged step. *Coast. Engng* **7** (4), 357–380.

MEI, C.C., STIASSNIE, M. & YUE, D.K.P. 1989 *Theory and Applications of Ocean Surface Waves: Part 1: Linear Aspects Part 2: Nonlinear Aspects*. World Scientific.

MORI, N. & JANSSEN, P.A.E.M. 2006 On kurtosis and occurrence probability of freak waves. *J. Phys. Oceanogr.* **36** (7), 1471–1483.

ONORATO, M., RESIDORI, S., BORTOLOZZO, U., MONTINA, A. & ARECCHI, F.T. 2013 Rogue waves and their generating mechanisms in different physical contexts. *Phys. Rep.* **528**, 47–89.

SERGEEVA, A., PELINOVSKY, E. & TALIPOVA, T. 2011 Nonlinear random wave field in shallow water: variable Korteweg–de Vries framework. *Nat. Hazards Earth Syst. Sci.* **11** (2), 323–330.

TAYFUN, M.A. 1980 Narrow-band nonlinear sea waves. *J. Geophys. Res.: Oceans* **85** (C3), 1548–1552.

TAYFUN, M.A. 1986 On narrow-band representation of ocean waves: 1. Theory. *J. Geophys. Res.: Oceans* **91** (C6), 7743–7752.

TOFFOLI, A., MONBALIU, J., ONORATO, M., OSBORNE, A.R., BABANIN, A.V. & BITNER-GREGERSEN, E. 2007 Second-order theory and setup in surface gravity waves: a comparison with experimental data. *J. Phys. Oceanogr.* **37** (11), 2726–2739.

TRULSEN, K. 2018 Rogue waves in the ocean, the role of modulational instability, and abrupt changes of environmental conditions that can provoke non equilibrium wave dynamics. In *The Ocean in Motion* (ed. M. G. Velarde *et al.*), pp. 239–247. Springer.

TRULSEN, K., RAUSTØL, A., JORDE, S. & BÆVERFJORD RYE, L. 2020 Extreme wave statistics of long-crested irregular waves over a shoal. *J. Fluid Mech.* **882**, R2.

TRULSEN, K., ZENG, H.M. & GRAMSTAD, O. 2012 Laboratory evidence of freak waves provoked by non-uniform bathymetry. *Phys. Fluids* **24** (9), 097101.

VIOTTI, C. & DIAS, F. 2014 Extreme waves induced by strong depth transitions: fully nonlinear results. *Phys. Fluids* **26** (5), 051705.

ZENG, H. & TRULSEN, K. 2012 Evolution of skewness and kurtosis of weakly nonlinear unidirectional waves over a sloping bottom. *Nat. Hazards Earth Syst. Sci.* **12** (3), 631–638.

ZHANG, J. & BENOIT, M. 2021 Wave–bottom interaction and extreme wave statistics due to shoaling and de-shoaling of irregular long-crested wave trains over steep seabed changes. *J. Fluid Mech.* **912**, A28.

ZHANG, J., BENOIT, M., KIMMOUN, O., CHABCHOUB, A. & HSU, H.C. 2019 Statistics of extreme waves in coastal waters: large scale experiments and advanced numerical simulations. *Fluids* **4**, 99.

ZHENG, Y.K., LIN, Z.L., LI, Y., ADCOCK, T.A.A., LI, Y. & VAN DEN BREMER, T.S. 2020 Fully nonlinear simulations of extreme waves provoked by strong depth transitions: the effect of slope. *Phys. Rev. Fluids* **5**, 064804.